

Modelling the Relationship Between Structural and Functional Connectomes

14016036

Abstract—The structural and functional intraconnectivity of the human brain is determined indirectly, leading to significant uncertainty and limiting the adoption of connectomics when researching various neurological disease states. Furthermore, even though a structural white matter connection is needed for distinct brain regions to functionally communicate, direct measurement of either connectome does not produce complimentary results.

In this report we evaluate various proposed linear models capable of linking the structural and functional connectome. We propose a model that incorporates second and third order indirect connectivity to allow functional data to be predicted at edges where no direct structural connection exists.

I. INTRODUCTION

For over a century it has been understood that the human cerebral cortex can be subdivided into various regions [1], with each region being delineated by differences in cellular composition or histological architecture [2]. These distinct cortical domains vary in neuronal activity for a given task - for example the primary visual cortex becomes more active during pattern recognition tasks [3] while the primary motor cortex activates during voluntary motion [4]. Note that these regions do not act in isolation - for example, during object observation tasks both aforementioned cortical areas are active simultaneously [5], [6]. This suggests that neural connections can link different cortical regions - a map of these connections is known as a connectome [7].

There are two different varieties of connectome - structural and functional. Structural connections are the physical white matter links between cortical regions and a structural connectome of the human brain can be generated using tractography. Diffusion weighted MRI (DW-MRI) is used to generate a complete map of fibre orientation throughout the brain: the anisotropic nature of white matter leads to a greater diffusion of water molecules along the neuronal tracks than across them [8], which can be directly measured with DW-MRI. A diffusion tensor can then be calculated for each voxel, the largest eigenvalue of which corresponds to the most probable orientation of white matter fibres [9]. Alignment of the diffusion tensor's eigenvectors can identify white matter tracts.

This diffusion tensor approach to tractography has significant disadvantages. Isotropic brain matter regions such as the cerebrospinal fluid filled ventricles do not produce strongly directional diffusion [10]. We can apply a fractional anisotropy (FA) threshold to ensure only strongly anisotropic regions

of brain are used to generate a structural connectome [11], where fractional anisotropy is a metric that measures the degree of anisotropic diffusion:

$$FA = \sqrt{\frac{1}{2} \frac{\sqrt{(\lambda_1 - \lambda_2)^2 + (\lambda_2 - \lambda_3)^2 + (\lambda_3 - \lambda_1)^2}}{\sqrt{\lambda_1^2 + \lambda_2^2 + \lambda_3^2}}} \quad (1)$$

with λ_1, λ_2 and λ_3 being the eigenvalues of the diffusion tensor.

Another issue with the simple diffusion tensor model is the inability to resolve crossing white matter fibers [12], a significant problem as the proportion of white matter in the human brain containing crossed fibers can be as high as 90% [13]. Various approaches circumvent this issue and allow resolution of multiple distinct fiber orientations within a given voxel [14], these include q-ball imaging [15], constrained spherical deconvolution [16] or a multicompartment approach, such as the ball and stick model [17]. These more complex fiber models allow researchers to determine the structural connectome using probabilistic, rather than deterministic, tractography. Probabilistic tractography helps account for the uncertainty inherent in fiber estimation.

The other type of connectome - the functional connectome - describes the “*functional interplay between different regions of the brain*” [18]. It is determined by resting state functional MRI (rsfMRI). Changes in cerebral blood oxygenation produce a varying blood oxygen level dependent (BOLD) signal which can then be detected in various cortical regions [18]. The signal similarity between different cortical regions is a covariance matrix that can then be determined using the shrinkage approach [19]. The shrinkage approach is a computationally efficient method to estimate covariance matrices that reduces the effect of outliers using a regularization parameter, λ [19].

Having generated the functional connectome a decision must be made on whether to keep or discard the data corresponding to negative connectivity [20]. Negative functional connectivity (NFC) represents an anticorrelated BOLD signal between two cerebral regions [21], and its origin has been the subject of significant debate [22]. We know NFC is not an artefact of any signal preprocessing or noise cancellation [23], but instead may be caused by an accumulated phased delay between different brain regions [22], or by the brain's organisation into distinct task-positive and task-negative networks [24].

Structural and functional connectivity are fundamentally

coupled - a physical neuronal connection must exist between any two cortical regions to allow for functional communication [25]. As both DW-MRI and rsfMRI are indirect measures of connectivity there is not a one-to-one mapping of the structural and functional connectome, instead a unifying model is needed [26].

When creating models to link the structural and functional connectome it is important to distinguish between direct and indirect connectivity. Regions in the cerebral cortex exhibit a “*small-world*” topology [27]. This means that each region is not connected to all other regions but instead expresses strong local connectivity or clustering, with particular nodes linking each cluster to each other (see Figure 1), ultimately meaning most nodes are only indirectly connected to the others.

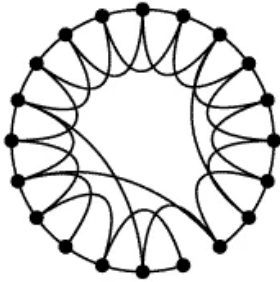


Figure 1: “*Small-world*” graph topology used to describe brain connectivity. Image taken from Watts and Strogatz [28].

A variety of brain connectivity metrics can be used to quantify the interconnectivity of the generated connectomes. We focus on four key metrics: edge density, global efficiency, mean shortest path length and clustering. The terms edge (E) and node (N) are frequently used in the study of brain connectivity, a node represents a cerebral region of interest and a edge represents either a structural or functional connection between nodes.

Edge density is a direct measure of the total connectivity of a brain network, representing the number of node connections against all potential connections [29] (see Equation 2). Recall that human brains are not fully connected and follow a “*small-world*” topology, as such typical values of edge density range between 10-30% [30].

$$\text{Edge density} = \frac{E}{N(N-1)} \quad (2)$$

Global efficiency and mean shortest path length are both measures of integration - they both essentially measure how many edges connect any two given nodes [31]. To be more specific, the global efficiency is defined as [32]:

$$\text{Global efficiency} = \frac{1}{N(N-1)} \sum_{i \neq j} \frac{1}{L_{i,j}} \quad (3)$$

where $L_{i,j}$ is the length of the shortest path between nodes i and j [30]. The mean characteristic path length is just the

inverse of the global efficiency and is defined as [28]:

$$\text{Mean shortest path length} = \frac{1}{N(N-1)} \sum_{i \neq j} L_{i,j} \quad (4)$$

While two different brain networks may have the same edge density, differences in topology may result in unique efficiency and mean shortest path lengths (see Figure 2).

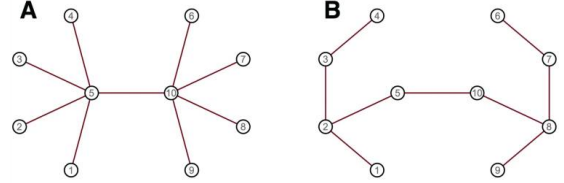


Figure 2: Two example brain networks with identical density but different efficiencies and mean shortest path lengths. Network A has a higher efficiency and lower mean shortest path length as on average less edges have to be crossed to reach any other node. Image taken from Clayden [33].

The final metric, the clustering coefficient, is a measure of segregation - it quantifies whether network nodes are separated into clusters or if good connectivity exists throughout the entirety of the brain. The global clustering coefficient is the average of all local clustering coefficients [30], which is determined by the number of triangular connections about a node (t_i) relative to the number of edges attached to that node (k_i) [34]:

$$\text{Global clustering coefficient} = \frac{1}{N} \sum \frac{2t_i}{k_i(k_i-1)} \quad (5)$$

In this report we start by evaluating the effect a fractional anisotropy threshold has on generating a structural connectome using various brain connectivity metrics. We then analyse the effectiveness of modifying λ when using the shrinkage method to generate functional connectivity maps, noting the effect of retaining or discarding negative correlations. Having done this we evaluate various linear models using data from multiple subjects, exploring various different methods of fitting the models to connectivity maps (across individual edges or whole subjects). We end by investigating the use of LASSO regularisation for model fitting.

II. METHODS

To evaluate the effect of thresholding fractional anisotropy, structural connectomes were generated from DW-MRI imaging data taken of a single healthy adult. Throughout this report the human cortex was segmented into the 68 labeled regions listed in the appendix (Table V). The R package TractoR [35] was used to generate binary undirected structural connectivity maps using 10,000 streamlines, if any streamline linked two cortical regions they were considered connected. A FA threshold was used to control where the seed could originate - ultimately eight different structural connectivity maps were generated with unique FA thresholds between 0.1

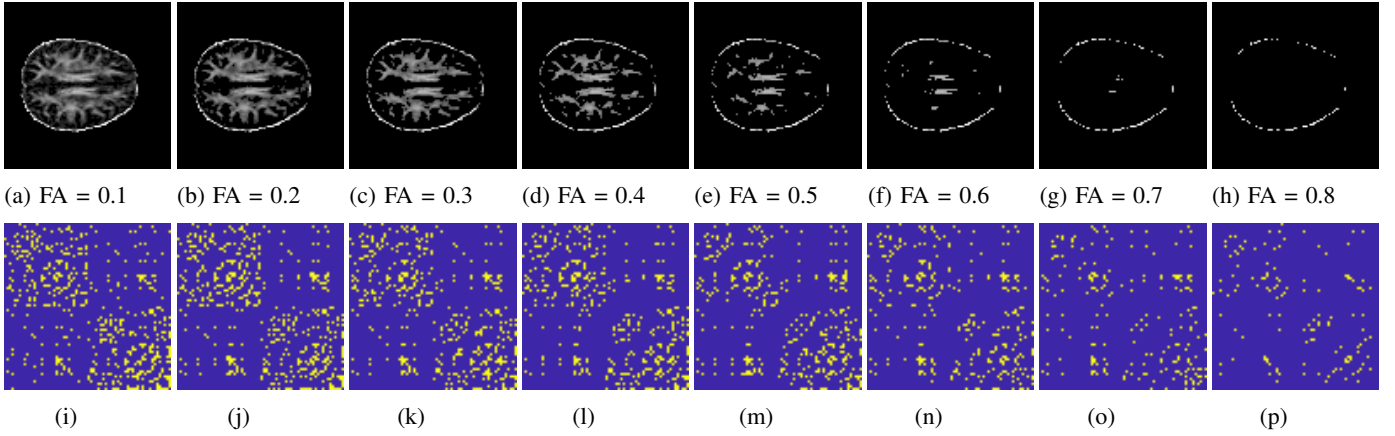


Figure 3: Generating binary undirected structural connectivity maps using different fractional anisotropy thresholds. Subfigures (a) to (h) show an axial thresholded FA map of the subject. During tractography seeds are able to originate in the shown areas. Subfigures (i) to (p) show the binary connectome. Blue = no streamline connects the two given regions while yellow = at least one does.

and 0.8 with increments of 0.1. The four aforementioned brain connectivity metrics were then calculated on these maps using the brain connectivity toolbox [34].

To generate functional connectivity maps we used rsfMRI data taken from the same subject. A modified shrinkage algorithm was used to estimate the resulting covariance matrix [19]. We varied the value of the shrinkage parameter, λ , to observe what effect regularisation would have on the connectome - we quantified this by binarizing the connectivity map with a cut-off of 0.1 and calculating brain connectivity metrics. We either kept or discarded edges with negative functional connectivity and evaluated the effect of doing so with the same four metrics.

We then use structural and functional data taken from 19 subjects to evaluate various linear models that link structural and functional data. Due to the “*small-world*” topology of brain networks, functional connectivity (f_{ij}) cannot be explained by purely direct structural connectivity (s_{ij}) so we define the indirect structural connectivity matrix (t_{ij}), which is representative of two nodes being connected along exactly two edges, as nodes 1 and 2 are connected along in Figure 2a. Stated more formally the indirect structural connectivity map, t_{ij} , consists of the greatest minimum weight in all available two-step chains:

$$t_{ij} = \max_k \{ \min\{s_{ik}, s_{kj}\} \} \text{ s.t. } s_{ik}, s_{kj} \neq 0. \quad (6)$$

We evaluate the following five linear models:

$$\begin{aligned} 1. f_{ij} &= \alpha_{ij} + \beta_{ij}s_{ij} \\ 2. f_{ij} &= \alpha_{ij} + \beta_{ij}s_{ij} + \gamma_{ij}s_{ij}^2 \\ 3. f_{ij} &= \alpha_{ij} + \beta_{ij}t_{ij} \\ 4. f_{ij} &= \alpha_{ij} + \beta_{ij}t_{ij} + \gamma_{ij}t_{ij}^2 \\ 5. f_{ij} &= \alpha_{ij} + \beta_{ij}s_{ij} + \gamma_{ij}t_{ij} \end{aligned} \quad (7)$$

Where α_{ij} , β_{ij} and γ_{ij} are the parameters for the linear model.

Cortical regions can be connected indirectly through more than two edges (e.g. nodes 1 and 6 in Figure 2) and so we propose a new linear model that incorporates second order indirect connectivity [36], u_{ij} , which is now defined as the greatest minimum weight in all available three-step chains:

$$f_{ij} = \alpha_{ij} + \beta_{ij}s_{ij} + \gamma_{ij}t_{ij}^2 + \delta_{ij}u_{ij}^3 \quad (8)$$

As the uncertainty of linking nodes increases with the number of edges crossed we square and cube the higher order indirect connectivity terms so they have a diminished impact on predicting the functional connectome.

We preform leave-one-out cross-validation to evaluate each linear model, and comparison between each model is aided by calculations of the Akaike information criterion (AIC) and Bayesian information criterion (BIC). We run these tests on the edges containing data from all models, as many edges have no functional data due to an absence of structural data. We also determine the structural connectivity density for each vertex for the direct and two/three step connectivity maps.

We fit the linear models in three different ways: across each edge independently, across every subject, and using each subject independently. We end by replacing our ordinary least squares method of model fitting with a more advanced LASSO based technique [37].

LASSO improves the predictive accuracy of a linear model by penalising potentially erroneous non-zero parameters using l_1 regularisation and is defined as [38]:

$$\hat{\beta}_k = \operatorname{argmin}_{\beta} \left(\frac{1}{2} \|Y - \beta X\|^2 + \lambda \|\beta\|_1 \right) \quad (9)$$

The value of λ controls the degree of regularisation and must be carefully chosen, usually using extensive cross-validation. Unfortunately, this was not possible due to computational constraints and so a value of $\lambda = 0.015$ was chosen from relevant literature [38].

III. RESULTS

The top row of Figure 3 shows what the thresholded fractional anisotropy maps look like through an arbitrary axial plane. These thresholded maps control where the 10,000 seeds for tractography can originate, producing the binary structural connectivity maps shown in the bottom row. We can now calculate the four brain connectivity metrics on these generated connectomes - the results are shown in Figure 4.

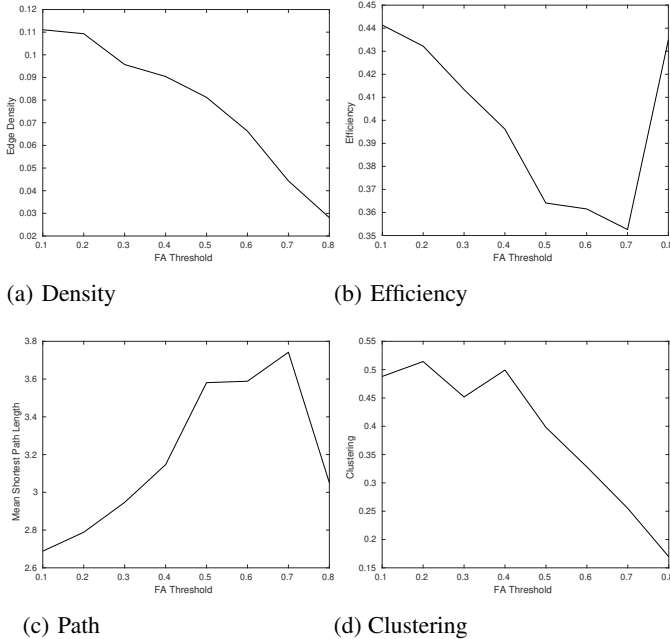


Figure 4: Edge density, efficiency, mean characteristic path length and clustering calculated for the structural connectivity maps found in Figure 3.

Using the shrinkage approach we were able to generate maps of structural connectivity from rsfMRI timecourse data measured in different brain regions (see Figure 5). We varied the shrinkage parameter, λ , to generate eight distinct connectomes. Note that some edges have a negative functional connectivity. We binarised these weighted functional connectivity maps using a value of 0.1, either keeping or discarding negative edges (see Figure 6). We are then able to calculate the same brain connectivity metrics when negative edges are retained or discarded, which we plot in Figure 7.

Confident in how maps of structural and functional connectivity are generated we can now move on to evaluating the various linear models. We start by fitting independently across each edge and comparing the generated functional connectome to one directly measured using rsfMRI for each subject. These results are plotted in Figure 9. We then go on to determine the AIC and BIC scores, and the residual sum of squares (RSS) for each model using leave-one-out cross-validation. These results are shown in Table I.

We also fit the linear model using a single set of coefficients

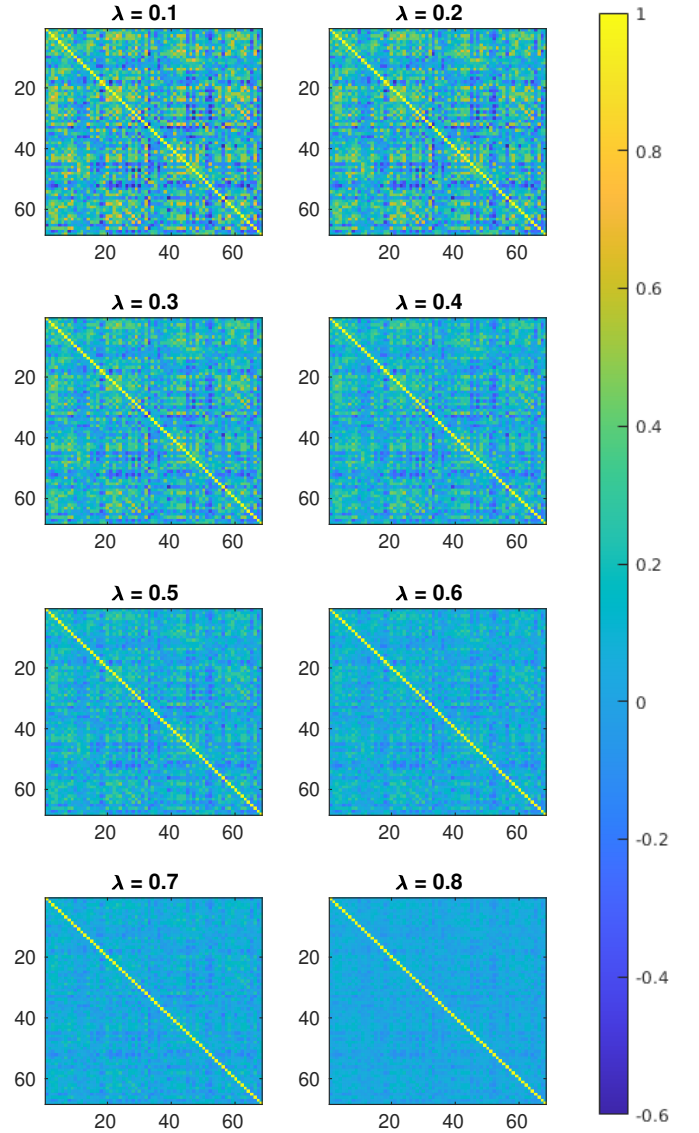
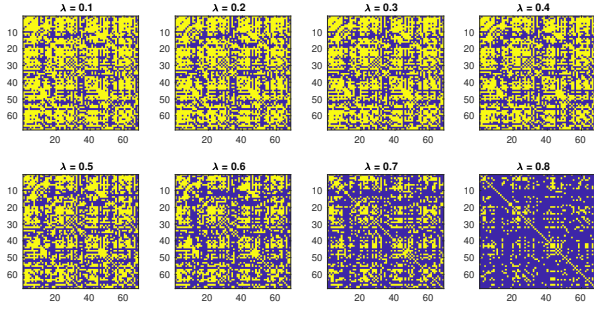


Figure 5: Functional connectivity maps generated using the shrinkage approach [19] for different values of the shrinkage parameter, λ . Note the presence of negative functional connectivity where some edges have a connectivity below zero.

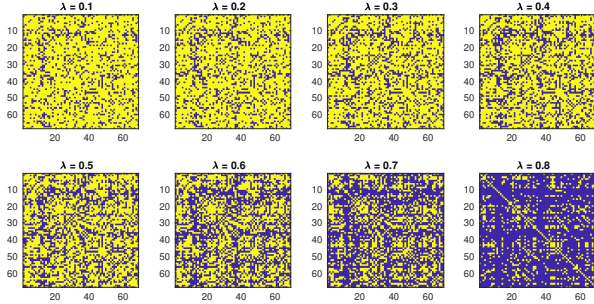
Table I: AIC, BIC and RSS as determined by model fitting across each edge independently.

Model	AIC	BIC	RSS
1) $f_{ij} = \alpha_{ij} + \beta_{ij}s_{ij}$	-105.63	-102.80	0.0460
2) $f_{ij} = \alpha_{ij} + \beta_{ij}s_{ij} + \gamma_{ij}s_{ij}^2$	-104.81	-101.03	0.0432
3) $f_{ij} = \alpha_{ij} + \beta_{ij}t_{ij}$	-105.55	-102.72	0.0462
4) $f_{ij} = \alpha_{ij} + \beta_{ij}t_{ij} + \gamma_{ij}t_{ij}^2$	-104.82	-101.04	0.0433
5) $f_{ij} = \alpha_{ij} + \beta_{ij}s_{ij} + \gamma_{ij}t_{ij}$	-104.88	-101.10	0.0431

for all edges. The data can be found in Table II.

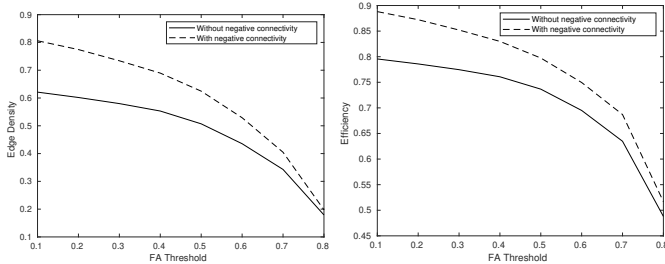


(a) Without negative edges.



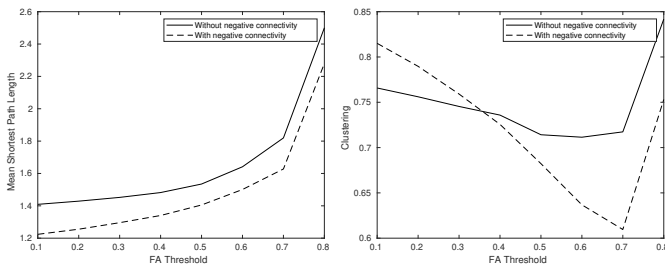
(b) Without negative edges.

Figure 6: Binary connectivity maps generated from the weighted functional connectome in Figure 5 using a threshold of 0.1. Negative edges were either kept or discarded.



(a) Density

(b) Efficiency



(c) Path

(d) Clustering

Figure 7: Edge density, efficiency, mean characteristic path length and clustering calculated from binarising functional connectivity maps found in Figure 5. Negative edges are either kept or discarded.

The direct (s_{ij}) and indirect (t_{ij}) structural connectivity maps are shown in Figure 8. We also show the three-step

Table II: AIC, BIC and RSS as determined by model fitting across all edges simultaneously.

Model	AIC	BIC	RSS
1) $f_{ij} = \alpha_{ij} + \beta_{ij}s_{ij}$	-101.15	-98.32	0.1553
2) $f_{ij} = \alpha_{ij} + \beta_{ij}s_{ij} + \gamma_{ij}s_{ij}^2$	-99.13	-95.35	0.1567
3) $f_{ij} = \alpha_{ij} + \beta_{ij}t_{ij}$	-101.13	-98.30	0.1572
4) $f_{ij} = \alpha_{ij} + \beta_{ij}t_{ij} + \gamma_{ij}t_{ij}^2$	-99.11	-95.34	0.1571
5) $f_{ij} = \alpha_{ij} + \beta_{ij}s_{ij} + \gamma_{ij}t_{ij}$	-99.14	-95.36	0.1512

indirect structural connectivity map (u_{ij}) used for our proposed sixth model (Equation 8). Having generated s_{ij} , t_{ij} and u_{ij} for each subject we are able to calculate the AIC, BIC and RSS, finding the AIC to be -104.01, the BIC to be -99.28 and the RSS to be 0.0405 - the lowest recorded RSS score of all the models.

A plot of structural connectivity density (generated by summing structural connectivity data across each vertex for all 19 subjects) has been created in Figure 10.

To highlight the danger of overfitting we now generate models using only one subject, evaluating the fitted model against all other subjects. This process can be thought of as leave- p -out cross validation where $p = \text{num. of subjects} - 1$. The results can be found in Table III.

Table III: AIC, BIC and RSS as determined by model fitting across all edges simultaneously. Only one subject was used to fit the model.

Model	AIC	BIC	RSS
1) $f_{ij} = \alpha_{ij} + \beta_{ij}s_{ij}$	-41.86	-43.87	1.672
2) $f_{ij} = \alpha_{ij} + \beta_{ij}s_{ij} + \gamma_{ij}s_{ij}^2$	-40.01	-42.00	1.645
3) $f_{ij} = \alpha_{ij} + \beta_{ij}t_{ij}$	-42.12	-43.48	1.666
4) $f_{ij} = \alpha_{ij} + \beta_{ij}t_{ij} + \gamma_{ij}t_{ij}^2$	-40.37	-41.78	1.679
5) $f_{ij} = \alpha_{ij} + \beta_{ij}s_{ij} + \gamma_{ij}t_{ij}$	-41.86	-41.61	1.599

To research the impact of regularisation we end by fitting all six proposed linear models on a per edge basis using LASSO regularisation and $\lambda = 0.0015$. The results are shown below in Table IV.

Table IV: AIC, BIC and RSS as determined by model fitting across each edge independently using LASSO with $\lambda = 0.0015$

Model	AIC	BIC	RSS
1) $f_{ij} = \alpha_{ij} + \beta_{ij}s_{ij}$	-102.65	-98.32	0.1523
2) $f_{ij} = \alpha_{ij} + \beta_{ij}s_{ij} + \gamma_{ij}s_{ij}^2$	-101.30	-95.35	0.1521
3) $f_{ij} = \alpha_{ij} + \beta_{ij}t_{ij}$	-101.98	-98.30	0.1523
4) $f_{ij} = \alpha_{ij} + \beta_{ij}t_{ij} + \gamma_{ij}t_{ij}^2$	-99.14	-95.34	0.1527
5) $f_{ij} = \alpha_{ij} + \beta_{ij}s_{ij} + \gamma_{ij}t_{ij}$	-99.44	-95.36	0.1510
6) $f_{ij} = \alpha_{ij} + \beta_{ij}s_{ij} + \gamma_{ij}t_{ij}^2 + \delta_{ij}u_{ij}^3$	-102.45	-97.40	0.1495

IV. DISCUSSION

The motivation behind FA thresholding during tractography is so that seeds start in voxels with clearly distinguishable

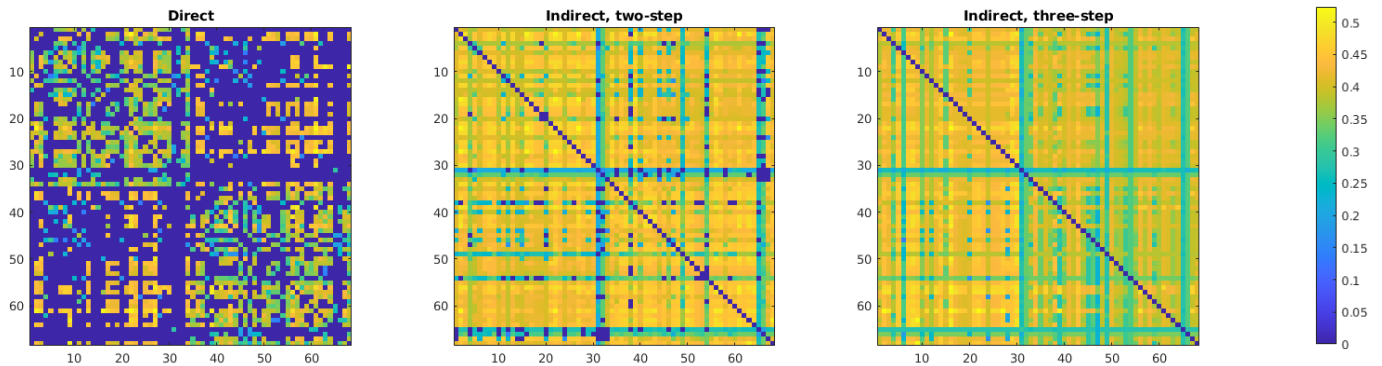


Figure 8: Structural connectivity maps showing directly connected nodes and indirectly connected nodes, with either two or three connecting edges.

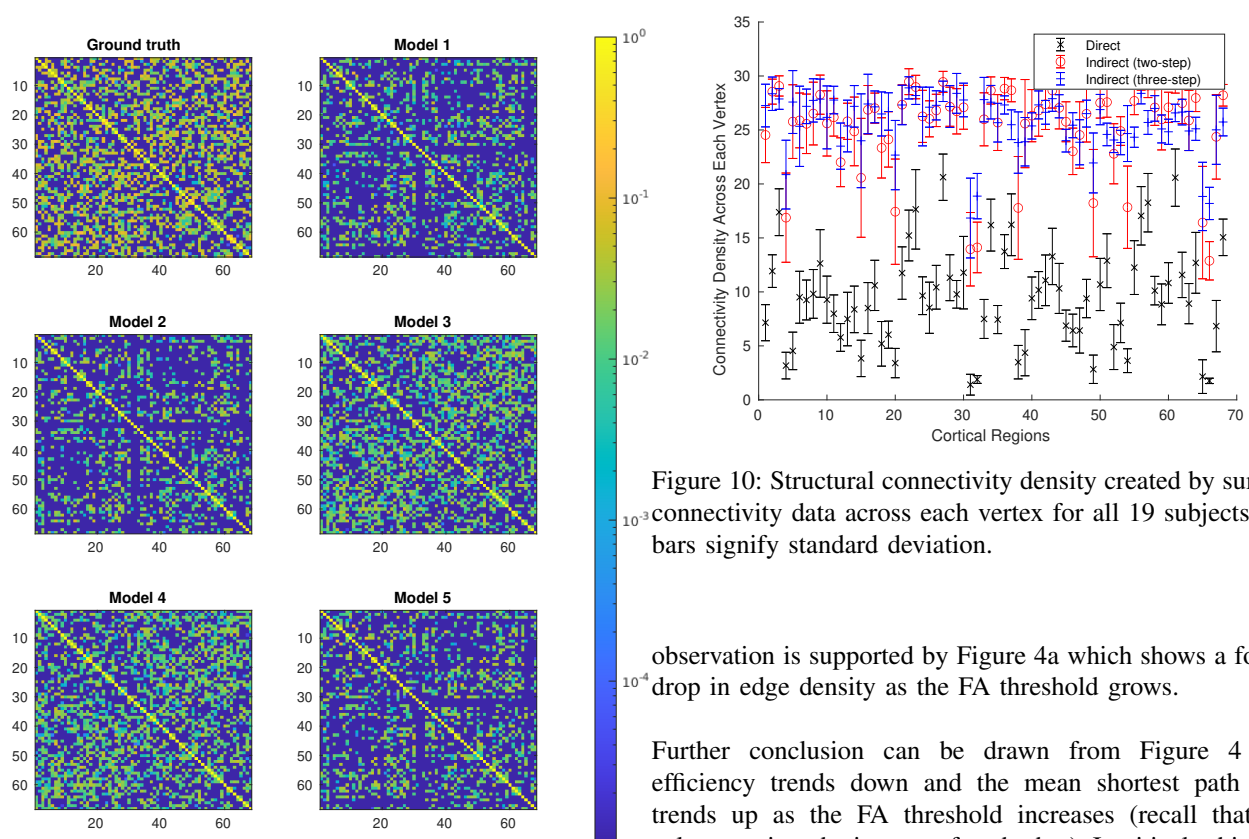


Figure 9: Functional connectivity maps generated by fitting the five linear models to direct and indirect structural connectivity maps. The connectome in the top left shows the ground truth determined using rsfMRI.

white matter tracts [39]. The low FA regions that are masked out often have no white matter entirely (like the ventricles) meaning that any streamline originating in such regions is highly likely to be unreliable.

We can immediately observe from Figure 3 that FA thresholding has a significant impact on the resultant connectivity map - with the structural connectome ultimately becoming sparser as the FA threshold increases. This

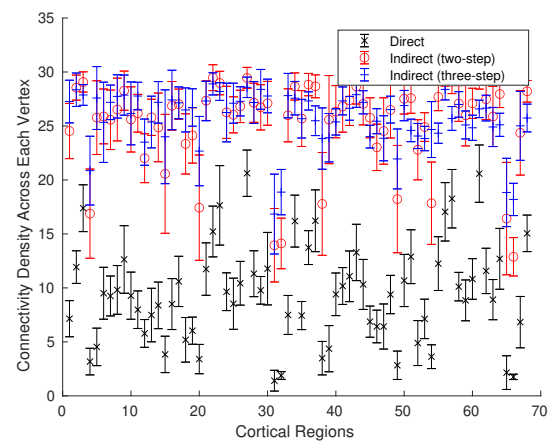


Figure 10: Structural connectivity density created by summing connectivity data across each vertex for all 19 subjects. Error bars signify standard deviation.

observation is supported by Figure 4a which shows a fourfold drop in edge density as the FA threshold grows.

Further conclusion can be drawn from Figure 4 - the efficiency trends down and the mean shortest path length trends up as the FA threshold increases (recall that these values are just the inverse of each other). Intuitively this seems sensible, the rising FA threshold severs potential connections, such that on average a more roundabout path must be taken to link two nodes. However, note the significant inversion that occurs when $FA = 0.8$. This arises at very high levels of thresholding as different brain regions are completely cut off from each other, and consequently have an infinite path length that does not get factored into the calculation of efficiency or mean shortest path length. In effect, we are now measuring path length in many small, isolated clusters rather than the entire brain, and the path length between any two nodes in the same cluster is on average much shorter.

Figure 4d shows a decrease in the clustering coefficient as the FA threshold rises. This metric quantifies clustering as the number of triangular connections about a node. As

the thresholding increases these triangles are broken apart as edges are masked out.

When using the shrinkage method to create functional connectivity maps selection of the shrinkage parameter, λ , has a significant impact on the generated connectome (see Figure 5). λ is a regularization parameter, and has the effect of pulling all model weights towards zero. Some degree of regularization is important to reduce the impact of outliers or inter-patient variability, but too much and the underlying data is eroded, which we can see when looking at the binarised connectivity maps (Figure 7).

Unsurprisingly, Figure 5 demonstrates that ignoring negative functional connectivity results in a much sparser connectome (see Figure 5). The same general trend with the brain connectivity metrics can be observed across Figure 7 - density decreases, although the extra negative edges produce a denser connectome at all values of λ . Efficiency falls and mean shortest path length rises, the negative edges allow for more possible connections between any two nodes, resulting in shorter routes on average, explaining the differences between connectomes generated with and without negative functional connectivity. The inversion in the clustering coefficient showing in Figure 7d is surprising. It may be explained by considering that the global clustering coefficient is the average of the local clustering about each node, as λ increases some nodal connections are completely severed such that they would no longer factor into the global average.

Ultimately, it may be more beneficial to consider the negative functional connectivity separate from the remaining functional connectome. This approach considers the “*task-positive*” and “*task-negative*” regions as separate networks [24] - such a technique has been used to study depression [40], dementia [41] and schizophrenia [42].

We now move onto the second part of the report - fitting and evaluating the various linear models against the data from the 19 subjects. In Figure 8 we give an example of the direct and indirect (both by 2 or 3 edges) structural connectivity maps that are generated for each subject. As expected, the direct connectivity map is the most sparse, the “*small-world*” theory explaining that any two nodes are most likely not actually directly connected, but instead are linked via multiple edges. We can observe this when looking at the indirect two and three-steps maps, which get progressively more well connected, and for the subject in Figure 8 no cortical region remains unconnected with fewer than three edges.

Using Figure 8 it is easy to see how structural and functional connectomes can be used as a research (or even diagnostic) aid for various neurological pathologies. An aberrantly connected brain region has been observed in those with depression [43], autism [37] or Alzheimer’s disease [44].

Figure 9 demonstrates the downside of relying wholly on direct structural connectivity to determine the functional

connectome - functional connectivity cannot be determined at edges without corresponding structural data, which is the majority of the brain. The greatest advantage to incorporating indirect connectivity data into a linear model is that more nodes are indirectly connected and so more functional data can ultimately be predicted. However, as we increase the order of indirect connectivity the uncertainty compounds as the number of edges increase, and local connectivity information is lost. Ultimately, we want some degree of indirect connectivity so that functional data can be generated on all edges, but the main contribution to the linear model should come from the direct connectivity maps. Our proposed linear model (Equation 8) does this by ramping up the power of higher order indirect connectivity terms such that their overall impact on the model is limited in cases where direct data exists.

To help visualise the progressive loss in useful information as the degree of indirect connectivity increases we plot Figure 10 - the structural connectivity density of the direct and indirect (two and three step) data. For all vertices the direct connection density was lower, which makes intuitive sense as there are less directly connected nodes. You also have the largest variability in density across each vertex, large data contrasts like this are critical to draw reliable conclusions from data. As we move to indirect data and the order increases we notice that the density converges towards a uniform value of ≈ 28 , with only a few poorly connected regions retaining a lower connectivity.

Unsurprisingly, fitting the linear models using data from only one subject produces the worse results. Even though Figure 10 shows us that connectivity trends can be drawn over an entire vertex (e.g. region x typically has more direct connections than region y), the intersubject variability is great enough that the predictive power of the linear models is greatly reduced (see Table III).

LASSO regularisation is one way to reduce the impact of subject variability during model fitting by reducing the effect of outliers through ℓ_1 regularisation. As we can see from Table IV, replacing the simple ordinary least squares approach with LASSO regularisation produces the models with the lowest AIC, BIC and RSS scores. The disadvantages to using LASSO include the need for careful selection of λ through cross-validation, something that was not possible in this report due to computational constraints.

V. CONCLUSIONS

Creating a link between structural and functional connectivity is a promising method to overcome the limitations that arise with direct measurement of the structural and functional connectome.

In this report we experiment with controlling the FA threshold and λ , key parameters in generating connectivity maps. We evaluate six linear models, using the AIC, BIC

and RSS scores for comparison. We find using a model that combines direct, and two+three stage functional connectivity produces the best fit. We also note that LASSO regularisation produces a significantly better fit than ordinary least squares.

REFERENCES

- [1] M. Strotzer, "One century of brain mapping using brodmann areas," *Clinical Neuroradiology*, vol. 19, no. 3, pp. 179–186, 2009.
- [2] S. M. Sherman and R. W. Guillery, *Functional connections of cortical areas: a new view from the thalamus*. MIT Press, 2013.
- [3] F. Tong, "Primary visual cortex and visual awareness," *Nature Reviews Neuroscience*, vol. 4, no. 3, pp. 219–229, 2003.
- [4] J. N. Sanes and J. P. Donoghue, "Plasticity and primary motor cortex," *Annual review of neuroscience*, vol. 23, no. 1, pp. 393–415, 2000.
- [5] R. Hari, N. Forss, S. Avikainen, E. Kirveskari, S. Salenius, and G. Rizzolatti, "Activation of human primary motor cortex during action observation: a neuromagnetic study," *Proceedings of the National Academy of Sciences*, vol. 95, no. 25, pp. 15 061–15 065, 1998.
- [6] J. Dushanova and J. Donoghue, "Neurons in primary motor cortex engaged during action observation," *European Journal of Neuroscience*, vol. 31, no. 2, pp. 386–398, 2010.
- [7] P. Hagmann, "From diffusion mri to brain connectomics," EPFL, Tech. Rep., 2005.
- [8] T. L. Chenevert, J. A. Brunberg, and J. G. Pipe, "Anisotropic diffusion in human white matter: demonstration with mr techniques in vivo," *Radiology*, vol. 177, no. 2, pp. 401–405, 1990.
- [9] P. J. Basser, J. Mattiello, and D. LeBihan, "Mr diffusion tensor spectroscopy and imaging," *Biophysical journal*, vol. 66, no. 1, pp. 259–267, 1994.
- [10] A. L. Alexander, J. E. Lee, M. Lazar, and A. S. Field, "Diffusion tensor imaging of the brain," *Neurotherapeutics*, vol. 4, no. 3, pp. 316–329, 2007.
- [11] L. J. O'Donnell and C.-F. Westin, "An introduction to diffusion tensor image analysis," *Neurosurgery Clinics*, vol. 22, no. 2, pp. 185–196, 2011.
- [12] K. H. Maier-Hein, P. F. Neher, J.-C. Houde, M.-A. Côté, E. Garyfalidis, J. Zhong, M. Chamberland, F.-C. Yeh, Y.-C. Lin, Q. Ji *et al.*, "The challenge of mapping the human connectome based on diffusion tractography," *Nature communications*, vol. 8, no. 1, pp. 1–13, 2017.
- [13] B. Jeurissen, A. Leemans, J.-D. Tournier, D. K. Jones, and J. Sijbers, "Investigating the prevalence of complex fiber configurations in white matter tissue with diffusion magnetic resonance imaging," *Human brain mapping*, vol. 34, no. 11, pp. 2747–2766, 2013.
- [14] K. K. Seunarine and D. C. Alexander, "Multiple fibers: beyond the diffusion tensor," in *Diffusion Mri*. Elsevier, 2014, pp. 105–123.
- [15] D. S. Tuch, "Q-ball imaging," *Magnetic Resonance in Medicine: An Official Journal of the International Society for Magnetic Resonance in Medicine*, vol. 52, no. 6, pp. 1358–1372, 2004.
- [16] J.-D. Tournier, F. Calamante, and A. Connelly, "Robust determination of the fibre orientation distribution in diffusion mri: non-negativity constrained super-resolved spherical deconvolution," *Neuroimage*, vol. 35, no. 4, pp. 1459–1472, 2007.
- [17] T. E. Behrens, H. J. Berg, S. Jbabdi, M. F. Rushworth, and M. W. Woolrich, "Probabilistic diffusion tractography with multiple fibre orientations: What can we gain?" *Neuroimage*, vol. 34, no. 1, pp. 144–155, 2007.
- [18] M. G. Preti, T. A. Bolton, and D. Van De Ville, "The dynamic functional connectome: State-of-the-art and perspectives," *Neuroimage*, vol. 160, pp. 41–54, 2017.
- [19] J. Schäfer and K. Strimmer, "A shrinkage approach to large-scale covariance matrix estimation and implications for functional genomics," *Statistical applications in genetics and molecular biology*, vol. 4, no. 1.
- [20] L. Zhan, L. M. Jenkins, O. E. Wolfson, J. J. GadElkarim, K. Nocito, P. M. Thompson, O. A. Ajilore, M. K. Chung, and A. D. Leow, "The significance of negative correlations in brain connectivity," *Journal of Comparative Neurology*, vol. 525, no. 15, pp. 3251–3265, 2017.
- [21] F. Parente and A. Colosimo, "Anticorrelations between active brain regions: An agent-based model simulation study," *Neural plasticity*, vol. 2018, 2018.
- [22] G. Chen, G. Chen, C. Xie, and S.-J. Li, "Negative functional connectivity and its dependence on the shortest path length of positive network in the resting-state human brain," *Brain connectivity*, vol. 1, no. 3, pp. 195–206, 2011.
- [23] C. Chang and G. H. Glover, "Effects of model-based physiological noise correction on default mode network anti-correlations and correlations," *Neuroimage*, vol. 47, no. 4, pp. 1448–1459, 2009.
- [24] M. D. Fox, A. Z. Snyder, J. L. Vincent, M. Corbetta, D. C. Van Essen, and M. E. Raichle, "The human brain is intrinsically organized into dynamic, anticorrelated functional networks," *Proceedings of the National Academy of Sciences*, vol. 102, no. 27, pp. 9673–9678, 2005.
- [25] H. Huang and M. Ding, "Linking functional connectivity and structural connectivity quantitatively: a comparison of methods," *Brain connectivity*, vol. 6, no. 2, pp. 99–108, 2016.
- [26] C. Stam, E. Van Straaten, E. Van Dellen, P. Tewarie, G. Gong, A. Hillebrand, J. Meier, and P. Van Mieghem, "The relation between structural and functional connectivity patterns in complex brain networks," *International Journal of Psychophysiology*, vol. 103, pp. 149–160, 2016.
- [27] O. Sporns and J. D. Zwi, "The small world of the cerebral cortex," *Neuroinformatics*, vol. 2, no. 2, pp. 145–162, 2004.
- [28] D. J. Watts and S. H. Strogatz, "Collective dynamics of small-world networks," *nature*, vol. 393, no. 6684, p. 440, 1998.
- [29] D. Tomasi and N. D. Volkow, "Functional connectivity density mapping," *Proceedings of the National Academy of Sciences*, vol. 107, no. 21, pp. 9885–9890, 2010.
- [30] M. Kaiser, "A tutorial in connectome analysis: topological and spatial features of brain networks," *Neuroimage*, vol. 57, no. 3, pp. 892–907, 2011.
- [31] C. Seguin, M. P. Van Den Heuvel, and A. Zalesky, "Navigation of brain networks," *Proceedings of the National Academy of Sciences*, vol. 115, no. 24, pp. 6297–6302, 2018.
- [32] V. Latora and M. Marchiori, "Efficient behavior of small-world networks," *Physical review letters*, vol. 87, no. 19, p. 198701, 2001.
- [33] J. D. Clayden, "Imaging connectivity: Mri and the structural networks of the brain," *Functional neurology*, vol. 28, no. 3, p. 197, 2013.
- [34] M. Rubinov and O. Sporns, "Complex network measures of brain connectivity: uses and interpretations," *Neuroimage*, vol. 52, no. 3, pp. 1059–1069, 2010.
- [35] J. D. Clayden, S. M. Maniega, A. J. Storkey, M. D. King, M. E. Bastin, C. A. Clark *et al.*, "Tractor: magnetic resonance imaging and tractography with r."
- [36] F. Deligianni, E. Robinson, C. F. Beckmann, D. Sharp, A. D. Edwards, and D. Rueckert, "Inference of functional connectivity from direct and indirect structural brain connections," in *2011 IEEE International Symposium on Biomedical Imaging: From Nano to Macro*. IEEE, 2011, pp. 849–852.
- [37] A. Irimia, C. M. Torgerson, Z. J. Jacokes, and J. D. Van Horn, "The connectomes of males and females with autism spectrum disorder have significantly different white matter connectivity densities," *Scientific reports*, vol. 7, p. 46401, 2017.
- [38] F. Deligianni, G. Varoquaux, B. Thirion, D. J. Sharp, C. Ledig, R. Leech, and D. Rueckert, "A framework for inter-subject prediction of functional connectivity from structural networks," *IEEE transactions on medical imaging*, vol. 32, no. 12, pp. 2200–2214, 2013.
- [39] A. D. Baur, T. Daqqaq, F. Colletini, T. Denecke, B. Hamm, T. Durmus, and M. Scheel, "Influence of fractional anisotropy thresholds on diffusion tensor imaging tractography of the periprosthetic neurovascular bundle and selected pelvic tissues: do visualized tracts really represent nerves?" *Acta Radiologica*, vol. 58, no. 4, pp. 472–480, 2017.
- [40] K. R. Cullen, M. K. Westlund, B. Klimes-Dougan, B. A. Mueller, A. Houry, L. E. Eberly, and K. O. Lim, "Abnormal amygdala resting-state functional connectivity in adolescent depression," *JAMA psychiatry*, vol. 71, no. 10, pp. 1138–1147, 2014.
- [41] A. Hafkemeijer, C. Möller, E. G. Dopper, L. C. Jiskoot, T. M. Schouten, J. C. van Swieten, W. M. van der Flier, H. Vrenken, Y. A. Pijnenburg, F. Barkhof *et al.*, "Resting state functional connectivity differences between behavioral variant frontotemporal dementia and alzheimers disease," *Frontiers in human neuroscience*, vol. 9, p. 474, 2015.
- [42] M.-E. Lynall, D. S. Bassett, R. Kerwin, P. J. McKenna, M. Kitzbichler, U. Muller, and E. Bullmore, "Functional connectivity and brain networks in schizophrenia," *Journal of Neuroscience*, vol. 30, no. 28, pp. 9477–9487, 2010.
- [43] M. S. Korgaonkar, A. Fornito, L. M. Williams, and S. M. Grieve, "Abnormal structural networks characterize major depressive disorder: a connectome analysis," *Biological psychiatry*, vol. 76, no. 7, pp. 567–574, 2014.
- [44] J. B. Pereira, D. Van Westen, E. Stomrud, T. O. Strandberg, G. Volpe, E. Westman, and O. Hansson, "Abnormal structural brain connectome in individuals with preclinical alzheimers disease," *Cerebral Cortex*, vol. 28, no. 10, pp. 3638–3649, 2018.

APPENDIX

Table V: The cortical segmentation used in this report.

Label	Region
1	banks superior temporal sulcus left
2	caudal anterior cingulate cortex left
3	caudal middle frontal gyrus left
4	cuneus left
5	entorhinal cortex left
6	fusiform gyrus left
7	inferior parietal gyrus left
8	inferior temporal gyrus left
9	cingulate gyrus isthmus left
10	lateral occipital cortex left
11	lateral orbitofrontal cortex left
12	lingual gyrus left
13	medial orbitofrontal gyrus left
14	middle temporal gyrus left
15	parahippocampal gyrus left
16	paracentral gyrus left
17	inferior frontal gyrus pars opercularis left
18	inferior frontal gyrus pars orbitalis left
19	inferior frontal gyrus pars triangularis left
20	pericalcarine cortex left
21	postcentral gyrus left
22	posterior cingulate gyrus left
23	precentral gyrus left
24	precuneus left
25	rostral anterior cingulate cortex left
26	rostral middle frontal gyrus left
27	superior frontal gyrus left
28	superior parietal gyrus left
29	superior temporal gyrus left
30	supramarginal gyrus left
31	frontal pole left
32	temporal pole left
33	transverse temporal gyrus left
34	insula left
35	banks superior temporal sulcus right
36	caudal anterior cingulate cortex right
37	caudal middle frontal gyrus right
38	cuneus right
39	entorhinal cortex right
40	fusiform gyrus right
41	inferior parietal gyrus right
42	inferior temporal gyrus right
43	cingulate gyrus isthmus right
44	lateral occipital cortex right
45	lateral orbitofrontal cortex right
46	lingual gyrus right
47	medial orbitofrontal gyrus right
48	middle temporal gyrus right
49	parahippocampal gyrus right
50	paracentral gyrus right
51	inferior frontal gyrus pars opercularis right
52	inferior frontal gyrus pars orbitalis right
53	inferior frontal gyrus pars triangularis right
54	pericalcarine cortex right
55	postcentral gyrus right
56	posterior cingulate gyrus right
57	precentral gyrus right
58	precuneus right
59	rostral anterior cingulate cortex right
60	rostral middle frontal gyrus right
61	superior frontal gyrus right
62	superior parietal gyrus right
63	superior temporal gyrus right
64	supramarginal gyrus right
65	frontal pole right
66	temporal pole right
67	transverse temporal gyrus right
68	insula right